Research Article

Green Synthesis of Biomass-Derived Carbon Quantum Dots from *Syzygium aromaticum* via Carbonization-Assisted Ultrasonication for a Selective Colorimetric Sensor of Ag^+ in Environmental Waters

Said Ali Akbar*
Department of Aquaculture, Faculty of Marine and Fisheries, Universitas Syiah Kuala, Banda Aceh, Indonesia

Ilham Zulfahmi
Department of Fisheries Resources Utilization, Faculty of Marine and Fisheries, Universitas Syiah Kuala, Banda Aceh, Indonesia

Ichsan Setiawan
Department of Marine Science, Faculty of Marine and Fisheries, Universitas Syiah Kuala, Banda Aceh, Indonesia

Zulkarnain Jalil
Department of Physics, Faculty of Mathematics and Natural Sciences, Universitas Syiah Kuala, Banda Aceh, Indonesia

Mohammad Mahmudur Rahman
Global Centre for Environmental Remediation (GCER), College of Engineering, Science and Environment, The University of Newcastle, Callaghan, NSW, Australia

Altaf Hussain Lahori
Department of Environmental Sciences, Sindh Madressatul Islam University, Karachi, Pakistan

* Corresponding author. E-mail: saidaliakbar@usk.ac.id DOI: 10.14416/j.asep.2025.09.011
Received: 20 May 2025; Revised: 8 July 2025; Accepted: 22 August 2025; Published online: 26 September 2025

Abstract
Carbon quantum dots (CQDs) were successfully synthesized from *Syzygium aromaticum* biomass using a carbonization-assisted ultrasonication approach. The resulting SA-CQDs exhibited a particle size of 3.31 nm, a quantum yield of 12.61%, and strong blue emission at 440 nm under 350 nm excitation. Spectroscopic analysis (FTIR, XPS, Raman) confirmed abundant oxygen- and nitrogen-containing functional groups, contributing to excellent aqueous dispersibility and optical responsiveness. The CQDs demonstrated high selectivity and sensitivity toward Ag^+ ions, with a distinct color change and an absorbance peak at 431 nm. A linear response was obtained in the 10–500 µM range (R^2 = 0.95579) with a low detection limit of 0.103 µM. Stability assessments revealed excellent fluorescence and absorbance retention across a broad range of pH, temperature, storage time, and light exposure. Recovery tests in tap and underground water showed 96.94–100.08% with RSD < 1%. This study supports the application of SA-CQDs as a green, cost-effective, and sensitive colorimetric probe for Ag^+ detection.

Keywords: Ag^+ detection, Carbon quantum dots, Colorimetric sensor, *Syzygium aromaticum*, Water monitoring

1 Introduction

Carbon quantum dots (CQDs) are emerging carbon-based nanomaterials (<10 nm) with strong photoluminescence, high solubility, biocompatibility, and chemical stability, making them valuable in sensing, bioimaging, optoelectronics, and environmental applications [1]–[3]. Their emission can be tuned through surface passivation, doping, or synthesis control [4]. Various synthesis methods exist, such as hydrothermal, ultrasonication, laser ablation, and pyrolysis [5]–[9]. Pyrolysis offers good graphitic cores but may be energy-intensive and less controlled [10], [11]. Carbonization-assisted ultrasonication improves dispersion, nucleation, and surface activation, yielding CQDs with enhanced fluorescence and a narrow size distribution.

Industrial and domestic effluents contribute significantly to water pollution, releasing hazardous substances—particularly heavy metals—into aquatic environments [12], [13]. These metals are toxic, non-biodegradable, and bioaccumulative, posing threats to ecosystems and human health. Traditional detection methods like AAS and ICP-MS are accurate but costly, complex, and impractical for on-site use [14], [15]. Carbon quantum dots (CQDs) offer a promising alternative due to their fluorescence, surface tunability, and water dispersibility, enabling sensitive detection of metal ions such as Cd^{2+}, Fe^{2+}, Ag^{+}, and Hg^{+} [16]. Silver ion (Ag^{+}) detection is especially important given its toxic effects on enzymes and organs [17]. CQDs interact with Ag^{+} via strong binding, inducing fluorescence quenching or color changes, making them ideal for green, real-time sensing [18].

Carbon-rich biomass and waste-derived materials have emerged as attractive precursors for the sustainable synthesis of carbon quantum dots (CQDs), offering an eco-friendly and cost-effective alternative to conventional methods that often require hazardous reagents and labor-intensive post-processing [19], [20]. Several studies have demonstrated the potential of biomass-based CQDs for the detection of silver ions (Ag^{+}), primarily through fluorescence-based mechanisms. For instance, CQDs synthesized from broccoli via one-step hydrothermal treatment achieved a limit of detection (LOD) as low as 0.5 µM for Ag^{+} due to efficient photoluminescence quenching [19]. Similarly, amine-functionalized graphene quantum dots derived from biowaste showed a fluorescence "switch-on" effect toward Ag^{+} in the presence of L-cysteine [21]. Nitrogen-doped CQDs from pomegranate juice enabled the detection of Ag nanoparticles with a LOD of 3.8×10^{-10} M through the inner filter effect and induced aggregation [20]. Other approaches include Ag-conjugated CDs from orange peel, with LOD ~0.85 µM for melamine detection via FRET-based quenching [22], and green-emissive N-CDs from *Lycium ruthenicum* capable of detecting Ag^{+} with an impressive LOD of 59 nM and smartphone-assisted visualization [23]. These findings collectively highlight the feasibility of transforming biomass into functional CQDs with selective and sensitive Ag^{+} detection capabilities, reinforcing the potential of green nanotechnology for environmental monitoring.

For the first time, *Syzygium aromaticum* (commonly referred to as clove) is utilized as a new and sustainable carbon source for the synthesis of CQDs using a straightforward method that combines thermal carbonization with ultrasonication [24]. SA is rich in eugenol (80–90% of its essential oil), along with tannins, flavonoids, and terpenes, which provide essential heteroatoms like oxygen and nitrogen for effective surface functionalization [24]. Its aromatic structure, with abundant hydroxyl and methoxy groups, enhances intrinsic fluorescence and structural stability [25], eliminating the need for additional chemical passivation. Moreover, SA is inexpensive and abundantly available in Indonesia, offering a cost-effective and eco-friendly route for CQD production. The resulting SA-derived CQDs exhibit strong, excitation-dependent photoluminescence, high water solubility, and excellent stability. Most importantly, they demonstrate selective and sensitive colorimetric detection of Ag^{+} ions in environmental water samples. This study represents the first report utilizing SA for green synthesis of CQDs, highlighting its potential for real-time silver ion monitoring in aquatic environments.

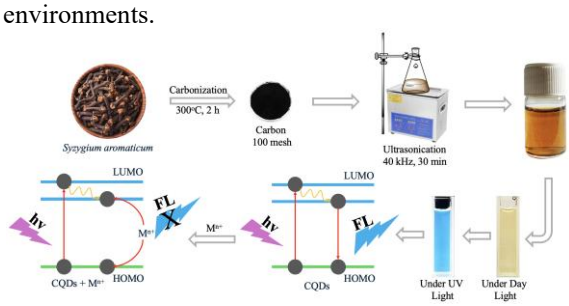

Figure 1: Schematic representation of SA-CQDs formation and application.

2 Materials and Methods

2.1 *Material*

The carbon precursor, *Syzygium aromaticum* (SA), was sourced from a local vendor at the traditional market in Ulee Kareng, Banda Aceh, Indonesia (5°33'03.2"N, 95°21'23.6"E). Chemicals including $Cr(NO_3)_3 \cdot 6H_2O$, H_2SO_4, HCl, $ZnCl_2$, $SnCl_2 \cdot 2H_2O$, $FeCl_3 \cdot 6H_2O$, $CdCl_2 \cdot H_2O$, $AgNO_3$, $HgCl_2$, $PbCl_2$, $Bi_5O(OH)_9(NO_3)_4$, $CoCl_2 \cdot 6H_2O$, $FeCl_2 \cdot 4H_2O$, $CuSO_4 \cdot 5H_2O$, dan $NiCl_2 \cdot 6H_2O$. were purchased from Sigma Aldrich. Ultrapure water (resistivity ~18.2 MΩ·cm at 25 °C), obtained from a Simplicity Millipore purification system, was used for all solution preparations throughout the study. Quinine TraceCERT® (Sigma-Aldrich) was utilized as a fluorescence standard for quantum yield determination.

2.2 *Synthesis of SA-CQDs*

Carbon quantum dots (CQDs) derived from *Syzygium aromaticum* (SA-CQDs) were synthesized through a modified two-step method combining thermal carbonization and ultrasonication, as adapted from reference [25] (see Figure 1). Initially, 100 grams of dried clove material were subjected to thermal treatment in a muffle furnace at 300 °C for 2 h to induce carbonization. The carbonized mass was then ground and sieved to achieve a uniform powder consistency. For the dispersion step, 1.25 grams of this powder were added to 40 mL of ultrapure water and sonicated in a water bath (40 kHz, 120 W) at room temperature for 30 min. The resulting mixture was passed through a 6 µm filter paper to remove coarse residues, and subsequently centrifuged at 4000 rpm for 1 hour to further purify the SA-CQDs suspension. The resulting supernatant was further purified by filtration through a 0.22 µm nylon membrane to obtain a transparent SA-CQDs solution, which was subsequently stored at 4 °C until use. To enhance the optical performance and yield of the carbon dots, essential synthesis variables—such as carbonization temperature, amount of precursor, and duration of sonication—were systematically optimized, as illustrated in Supplementary Figure S1.

2.3 *Instrumentation*

A comprehensive characterization of the synthesized SA-CQDs was performed using various analytical techniques. Carbonization of *Syzygium aromaticum* was carried out in a Nabertherm LE 1/11 muffle furnace, followed by dispersion using an EECOO MH-020S ultrasonic cleaner (40 kHz) and separation via centrifugation (DLAB DM0424). UV-induced fluorescence was observed under a Joyko FL-90UV lamp (365 nm), while photoluminescence spectra were recorded with a Shimadzu RF-5301PC spectrofluorometer. DLS and zeta potential were measured using a Horiba SZ-100z analyzer. FTIR analysis was conducted using a ThermoFisher Nicolet iS50, and UV–Vis absorbance using a ThermoFisher AQUAMATE 8000. Morphological and crystallographic structures were examined via TEM, HRTEM, and SAED using a Tecnai G2 Supertwin microscope. Raman spectra were acquired with a LabRam HR (Horiba), and XPS analysis was conducted on a Kratos AXIS SUPRA PLUS/ESCA system. These combined analyses confirmed the structural integrity, functional groups, and optical properties of SA-CQDs, supporting their potential in sensing applications.

2.4 *Quantum yield calculation*

The fluorescence quantum yield (QY) of the synthesized SA-CQDs was experimentally determined using quinine as a reference fluorophore. In this assessment, quinine (QY = 54%) was dissolved in 0.1 M H_2SO_4, while the SA-CQDs were diluted in ultrapure water. Both solvents have a refractive index of 1.33, ensuring consistency in optical conditions [16]. Solutions of the SA-CQDs and quinine were adjusted to have a matched absorbance of 0.05 at 350 nm, using a 1 cm pathlength quartz cuvette. Fluorescence emission spectra were recorded at an excitation wavelength of 350 nm, and the integrated fluorescence intensities were used to calculate the QY based on a comparative method. The following Equation (1) was applied:

$$QY_x = QY_y \left(\frac{A_y}{A_x}\right)\left(\frac{I_x}{I_y}\right)\left(\frac{\eta_x^2}{\eta_y^2}\right) \quad (1)$$

Here, QY refers to the quantum yield, A indicates the absorbance, I represents the integrated fluorescence intensity, and η corresponds to the refractive index of the solvent. The subscripts x and y denote the test sample (SA-CQDs) and the reference standard (quinine), respectively.

2.5 Detection of Ag^+ Ions

The ability of SA-CQDs to function as a colorimetric sensor for Ag^+ ions was investigated through UV–Vis spectrophotometric measurements in the 200–800 nm range. In a standard assay, 100 µL of SA-CQDs solution was mixed with 900 µL of ultrapure water, and then different metal ions—such as Ni^{2+}, Cu^{2+}, Fe^{2+}, Co^{2+}, Bi^{3+}, Pb^{2+}, Hg^{2+}, Cd^{2+}, Fe^{3+}, Sn^{2+}, Zn^{2+}, Cr^{3+}, and Ag^+—were added to achieve a final concentration of 500 µM. [16]. The mixtures were briefly sonicated (30 seconds, 40 kHz), adjusted to neutral pH (~7), and allowed to equilibrate at room temperature (~25 °C) for approximately 5 min prior to spectral analysis. The goal was to evaluate selective optical changes in the absorbance profiles of SA-CQDs upon interaction with different metal ions. Among the tested ions, Ag^+ uniquely induced a noticeable increase in absorbance intensity, accompanied by the formation of a distinct brown coloration in solution. To further examine selectivity, Ag^+ was also introduced in the presence of competing ions to assess interference effects, with results indicating minimal signal disruption. For sensitivity analysis, increasing concentrations of Ag^+ (10–500 µM) were added to the SA-CQDs solution under identical conditions. The resulting gradual enhancement in absorbance, particularly around 431 nm, confirmed a concentration-dependent response, establishing the viability of SA-CQDs as an efficient and selective colorimetric sensor for Ag^+ in aqueous environments.

2.6 Colorimetric *detection of Ag^+ in real water samples*

To assess the practical utility of SA-CQDs as a colorimetric sensor, their performance in detecting Ag^+ ions was evaluated using unfiltered tap and groundwater samples. A 500 µL aliquot of each water sample was spiked with standard Ag^+ solutions to yield final concentrations ranging from 10 to 300 µM, followed by mixing with SA-CQDs. The resulting mixtures were analyzed via UV–Vis spectroscopy to monitor absorbance changes. Recovery percentages were calculated to determine the accuracy of Ag^+ detection in real matrices, using standard comparison methods. The results confirmed the suitability of SA-CQDs for monitoring Ag^+ in environmental water samples.

2.7 *Data processing and analysis*

All numerical data were processed and visualized using Origin Pro 2024, while statistical evaluations were performed using SPSS version 26. All measurements were conducted in quadruplicate (n = 4), and results are expressed as mean ± standard deviation (SD). For validation, relative standard deviation (RSD) values were calculated to assess measurement precision. For comparative studies involving multiple groups, one-way ANOVA followed by Tukey's post hoc test was applied, with a significance threshold of p-value < 0.05. Recovery and precision analyses for Ag^+ detection in real water samples were used to evaluate method reliability (see Table 2), with recovery values ranging from 96.94% to 100.08% and RSDs below 0.7%, indicating excellent reproducibility. Additionally, ImageJ software was used to analyze HRTEM and SAED images to determine particle morphology and size distribution of the SA-CQDs.

3 Results and Discussion

3.1 *Determination of optimal preparation parameters*

The synthesis parameters for SA-CQDs were optimized through systematic variation of carbonization temperature, precursor mass, and sonication time, with detailed results provided in Supplementary Figure S1. Among the tested conditions, carbonization temperatures ranging from 200 °C to 500 °C revealed that 300 °C yielded the highest fluorescence intensity (Figure S1(a)), likely due to sufficient carbon core formation while preserving surface functional groups. Additionally, varying the mass of *Syzygium aromaticum* biomass from 0.2 g to 2.0 g indicated that 1.2 g was the optimal dosage, beyond which fluorescence intensity plateaued (Figure S1(b)), suggesting saturation of carbonization efficiency. Furthermore, the effect of sonication time from 5 to 60 min showed maximum intensity at 40 min (Figure S1(c)), indicating an effective dispersion and surface activation of CQDs. These optimized conditions—300 °C for 2 h, 1.2 g precursor, and 40 min sonication—were consistently used throughout the synthesis process and are supported by the fluorescence stability shown in Fig. S1d. This strategic optimization ensured reproducible synthesis of high-quality SA-CQDs.

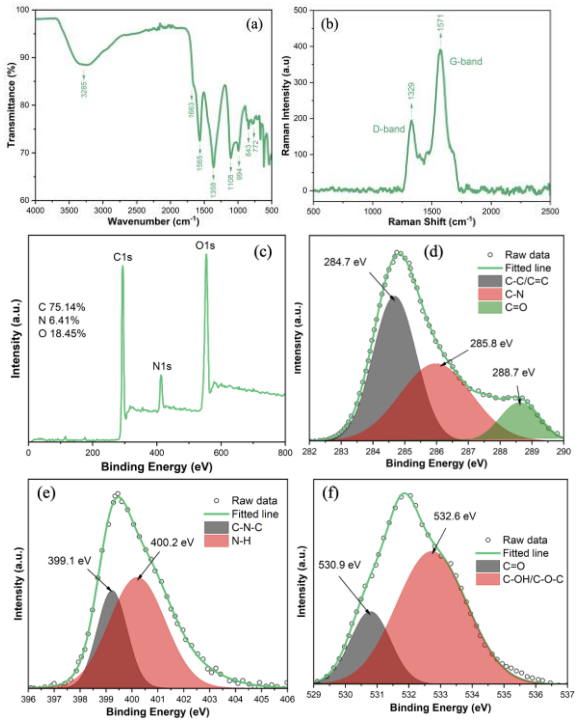

Figure 2: FTIR spectrum of SA-CQDs (a), Raman spectrum (b), full-survey XPS spectrum (c), and high-resolution deconvoluted spectra of (d) C1s, (e) N1s, and (f) O1s, revealing surface functional groups and elemental composition.

3.2 *Physicochemical properties of SA-CQDs*

Fourier-transform infrared (FTIR) and Raman spectroscopy were employed to examine the chemical composition and surface groups of the synthesized SA-CQDs. As shown in the FTIR spectrum (Figure 2(a)), distinct absorption bands were observed, confirming the existence of oxygen-based functional groups on the CQD surface. A broad peak centered around 3285 cm^{-1} corresponds to O–H or N–H stretching vibrations, indicating the presence of hydroxyl and amine groups, which contribute to the material's water dispersibility and play a key role in metal ion binding [26]. Distinct peaks appearing at 1565 cm^{-1} and 1358 cm^{-1} are associated with C=C stretching in aromatic structures and C–N or C–O vibrational modes, respectively. These features suggest the occurrence of partial graphitic domains and the incorporation of heteroatoms within the carbon matrix [27]–[29]. The absorption band near 1663 cm^{-1} is likely associated with the stretching vibration of carbonyl (C=O) groups. Meanwhile, the signals detected at 994, 1108, 843, and 772 cm^{-1} are attributed to C–H bending, symmetric stretching of C–O–C bonds, and out-of-plane bending vibrations of aromatic rings, respectively [30]. Raman spectroscopy provided additional evidence of graphitic structures and inherent defects in the carbon framework. The spectrum displayed two prominent features: the D-band at 1329 cm^{-1}, which is linked to sp^3-hybridized carbon atoms and lattice imperfections, and the G-band at 1571 cm^{-1}, indicative of sp^2-bonded carbon typical of graphitic domains [31] (Figure 2(b) and Figure S2)). It is worth noting that the G-band exhibited higher intensity compared to the D-band, indicating a greater extent of graphitic ordering and the presence of well-structured aromatic regions within the carbon network [32]. Although a direct comparison with the raw SA biomass was not conducted in this study, the observed spectral features of SA-CQDs are consistent with previous reports on CQDs derived from nitrogen- and oxygen-rich bioprecursors. This suggests that the key functional groups and graphitic structures were successfully retained or transformed during the carbonization-assisted ultrasonication process.

The elemental composition and surface chemistry of the synthesized SA-CQDs were further examined through X-ray Photoelectron Spectroscopy (XPS), as shown in the survey and high-resolution spectra. The survey spectrum revealed dominant peaks corresponding to C1s, N1s, and O1s, with atomic percentages of 75.14% for carbon, 6.41% for nitrogen, and 18.45% for oxygen, indicating successful incorporation of heteroatoms into the carbon matrix (Figure 2(c)) [33]. The high carbon content reflects the carbonaceous backbone of the CQDs, while the presence of nitrogen and oxygen supports the abundance of surface functional groups derived from the clove precursor [34]. The deconvoluted C1s spectrum shows multiple components: a primary peak at 284.6 eV attributed to graphitic sp^2 carbon (C–C/C=C), a peak at 285.9 eV assigned to C–N bonding, and a weaker signal at 287.5 eV corresponding to C=O groups (Figure 2(d)) [35]. Additional minor contributions appear at 288.6 eV and 287.5 eV, representing C–O and C=O functionalities, respectively. This distribution confirms the presence of various oxygen-containing moieties critical for metal ion coordination and aqueous dispersibility [36]. The N1s spectrum is resolved into three distinct peaks: 399.2 eV (C–N–C), 400.2 eV (N–H), and 401.5 eV (C=N), indicating multiple nitrogen bonding environments, which may arise from amine, imine, or pyrrolic

structures introduced during the carbonization of nitrogen-containing biomolecules in *Syzygium aromaticum* (Figure 2(e)) [37]. These nitrogen functionalities are known to improve the photoluminescence quantum yield and serve as electron donors in metal sensing mechanisms [38]. The O1s spectrum presents two primary peaks: one at 530.7 eV associated with carbonyl (C=O) groups, and a broader peak at 532.7 eV corresponding to hydroxyl and ether (C–OH/C–O–C) functionalities (Figure 2(e)) [39], [40]. The significant contribution of oxygen-based groups reinforces the hydrophilic character of the SA-CQDs and their affinity toward metal ions such as Ag^+ through electrostatic interaction and surface complexation. These functional groups were not introduced through chemical passivation or surface modification, but rather originated naturally from the phytochemical constituents of *Syzygium aromaticum*. During the carbonization process, compounds such as eugenol, flavonoids, and tannins—rich in hydroxyl, methoxy, and amino functionalities—undergo thermal transformation, leading to their partial incorporation into the carbon matrix of the CQDs. This intrinsic chemical composition of the precursor thus imparts the SA-CQDs with a variety of heteroatom-containing surface groups essential for water solubility, fluorescence activity, and selective metal ion coordination.

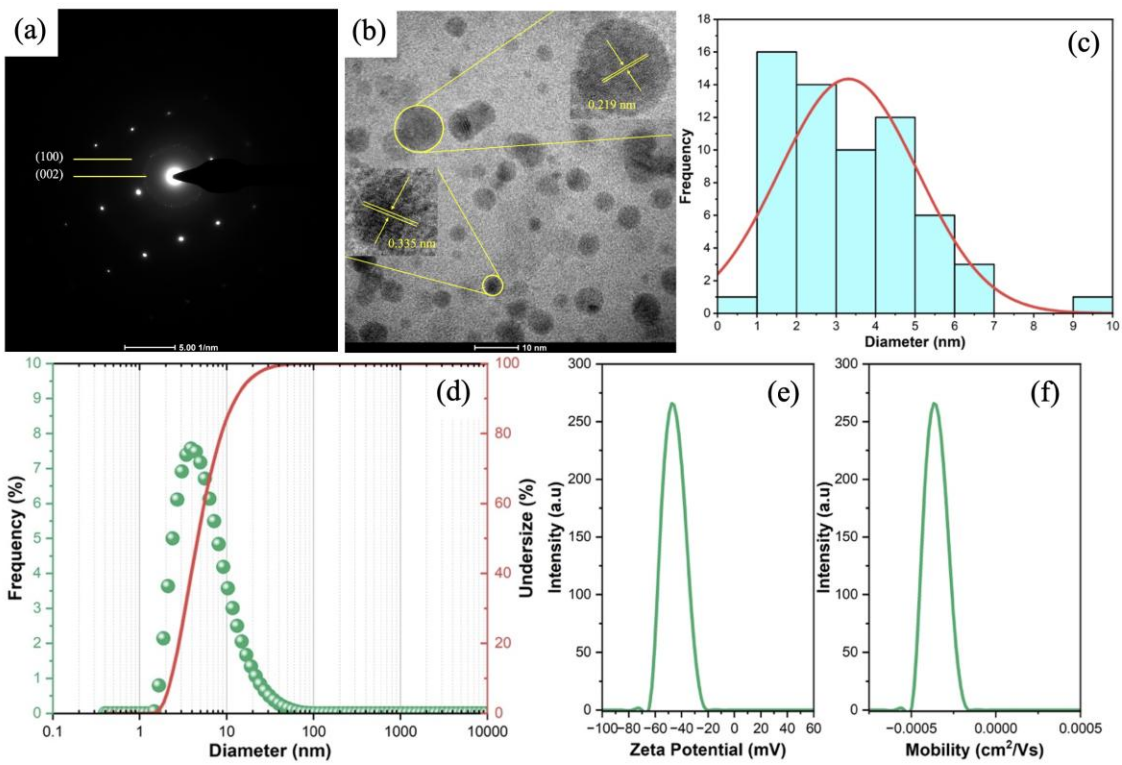

Figure 3: (a) SAED Pattern (b) HR-TEM image of the CQDs (c) the size distribution of particles (d) Hydrodynamic diameter by DLS (e) the zeta potential and (f) the electrophoretic mobility of CQDs.

The HRTEM image clearly revealed quasi-spherical nanoparticles with well-dispersed morphology and uniform contrast, indicating homogeneous synthesis. Lattice fringe measurements from the HRTEM micrograph showed two distinct interplanar spacings of approximately 0.335 nm and 0.219 nm, corresponding to the (002) and (100) planes of graphitic carbon, respectively (Figure 3(a) and (b)) [16], [41]. These crystalline features are further supported by the SAED pattern, which displayed a characteristic ring pattern with diffraction spots indexed to the same (002) and (100) planes (Table S1), confirming partial graphitic structure within the amorphous carbon matrix of the CQDs [42], [43]. The particle size histogram obtained from TEM images showed a predominant diameter centered around 3.31 nm, in good agreement with the DLS-derived size distribution, where the most frequent hydrodynamic

diameter was 3.89 nm (Figure 3(c) and (d)). The slight difference is attributed to the solvation shell and Brownian motion effects captured during DLS measurement, which tends to slightly overestimate particle size [44]. These values indicate that the SA-CQDs possess nanometric dimensions suitable for quantum confinement effects and colloidal stability in aqueous media.

The surface charge characteristics and colloidal stability of the SA-CQDs were further explored through zeta potential and electrophoretic mobility analyses. The zeta potential distribution revealed a prominent peak at –47.52 mV, with an intensity of 265.87 a.u., indicating strong electrostatic repulsion among particles in suspension (Figure 3(e)) [16]. This high negative surface charge is associated with the abundance of oxygen- and nitrogen-containing functional groups on the SA-CQDs surface, such as –COOH, –OH, and $–NH_2$, which were previously confirmed via FTIR and XPS analyses. Such a highly negative zeta potential reflects excellent colloidal stability in aqueous environments, minimizing the risk of particle aggregation over time [45]. In parallel, the electrophoretic mobility measurement showed a peak value of $–3.6735 \times 10^{-4}$ cm²/V·s, which is consistent with the strong negative surface charge and provides further insight into the behavior of these nanomaterials under an applied electric field (Figure 3(f)). The mobility data also suggest good uniformity of charge distribution on the surface, reinforcing the monodispersity observed from DLS and TEM results.

3.3 *Optical properties of SA-CQDs*

The optical properties of the synthesized SA-CQDs were investigated through UV–Vis absorption and fluorescence spectroscopy. The UV–Vis spectrum exhibited two distinct absorption bands at 252 nm and 324 nm, which are attributed to π–π* transitions of conjugated C=C bonds and n–π* transitions of non-bonding electrons from heteroatoms such as oxygen or nitrogen to π* orbitals, respectively (Figure 4(a) and Figure S3)) [46]. These features are characteristic of carbon-based nanostructures with aromatic domains and surface functionalities [47]. Excitation-dependent fluorescence behavior was observed, as evidenced by the red-shift in emission maxima upon varying excitation wavelengths from 300 nm to 500 nm (Figure 4(b) and Figure S4). This phenomenon is typical of carbon quantum dots and reflects a heterogeneous distribution of surface states and particle sizes [48]. Notably, the maximum emission intensity occurred at 440 nm when excited at 350 nm, consistent with the excitation spectrum peak. The strong blue fluorescence under UV illumination (inset image) further supports the presence of emissive trap states or surface defects contributing to radiative recombination. The broad and asymmetric emission profiles suggest multiple emissive centers within the CQDs structure, likely arising from different oxygen- and nitrogen-containing groups, which were previously confirmed via FTIR and XPS analyses.

The chromaticity coordinates and fluorescence lifetime of SA-CQDs were evaluated to gain deeper insight into their optical emission behavior. The CIE 1931 chromaticity diagram shows that the emission coordinates of SA-CQDs under 350 nm excitation are located at (0.155, 0.103), corresponding to the deep blue region of the visible spectrum (Figure 4(c)). This positioning reflects the high purity and consistency of blue luminescence observed under UV light, which is favorable for applications in optoelectronics and sensing [49]. Furthermore, the time-resolved photoluminescence (TRPL) decay profile was fitted using a double-exponential model, yielding two lifetime components: a short-lived component of 3.09 ns and a longer-lived component of 11.59 ns (Figure 4(d)). The average fluorescence lifetime (τ_{avg}) was calculated to be 3.86 ns, indicating that the emission predominantly arises from radiative recombination of excitons at surface defect states [50].

The optical activity observed in the 300–500 nm excitation range and the corresponding 400–520 nm emission range indicates a tunable and excitation-dependent photoluminescence behavior, which is crucial for designing wavelength-selective sensing platforms. Among the range tested, excitation at 350 nm and emission at 440 nm provided the most intense and stable fluorescence, making this condition the optimal window for practical applications. The strong fluorescence under 350 nm excitation is particularly advantageous for metal ion detection, including Ag^+ sensing, where signal clarity and reproducibility are critical. The observed photophysical properties are influenced by factors such as particle size distribution, surface passivation, and the presence of electron-rich functional groups derived from *Syzygium aromaticum*, which modulate the electronic transitions and trap-state emissions. This optical behavior highlights the versatility of SA-CQDs in fluorescent probe development and reinforces their applicability in real-time environmental monitoring systems or bioimaging applications.

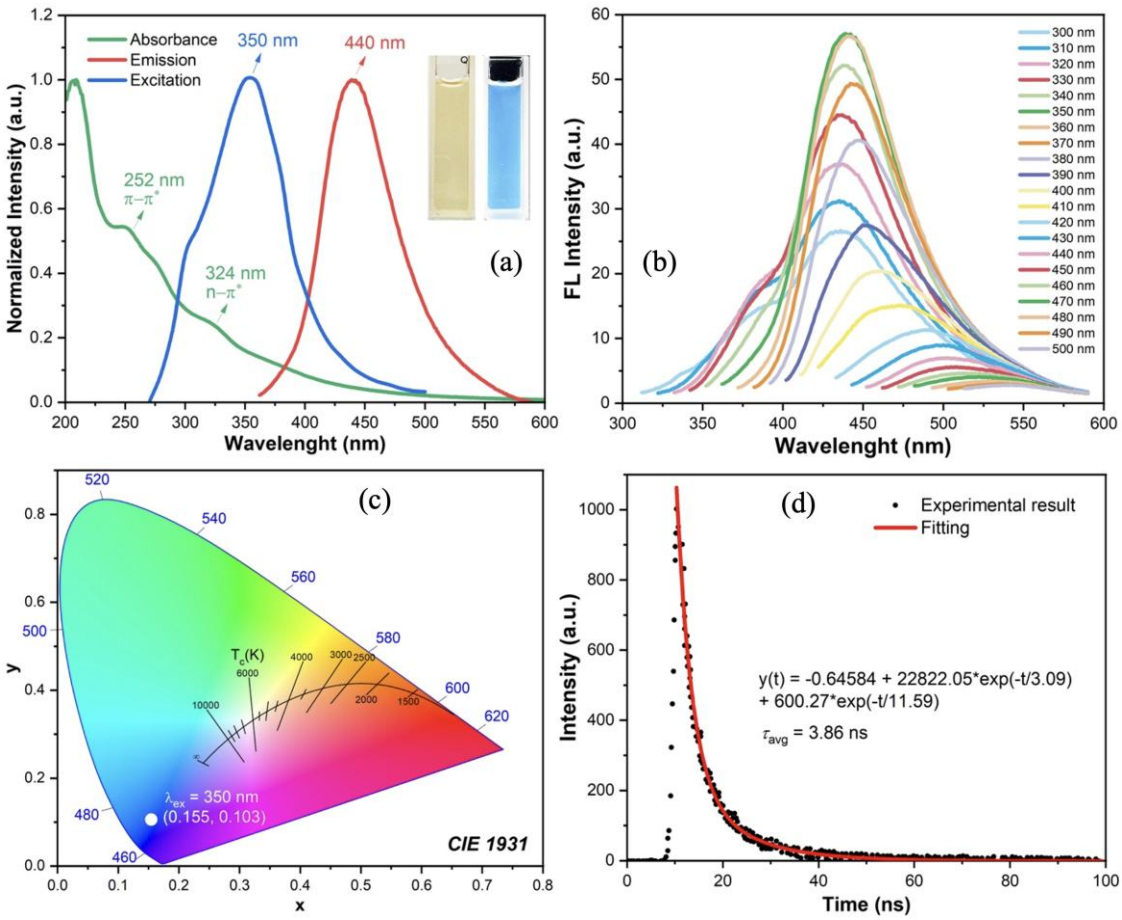

Figure 4: (a) fluorescence excitation and emission spectra of SA-CQDs (b) fluorescence spectra of SA-CQDs at various excitation wavelengths from 300 to 500 nm with a 10 nm increase (c) CIE chromaticity diagram (d) fluorescence decay curve of CQDs fitted by two-order exponential functions.

3.4 *Optical Stability of SA-CQDs*

The optical stability of SA-CQDs was systematically assessed under various environmental conditions to determine their robustness and applicability in real-world sensing systems. During a 10-day storage test at room temperature, the fluorescence intensity (F/F_0) of the SA-CQDs remained above 0.95, indicating minimal photobleaching or aggregation over time (Figure S5(a)). Absorbance stability (A/A_0 at 431 nm) was also preserved throughout the test period, demonstrating that the structural and electronic integrity of the CQDs was not compromised during storage [51]. The pH-dependent response of the CQDs was examined in the range of pH 3 to 10 (Figure S5(b)). The fluorescence performance remained stable and peaked near pH 7, suggesting that the surface functional groups (e.g., –COOH, –OH, $–NH_2$) on the CQDs maintain optimal emissive properties under neutral conditions. However, slight quenching at extreme pH levels was observed, possibly due to protonation or deprotonation of these groups. Interestingly, the colorimetric response (A/A_0) remained strong even in alkaline pH, suggesting that the absorbance-based Ag^+ detection mechanism is less affected by pH variation compared to the fluorescence process [52]–[54].

Thermal and photostability studies further confirmed the resilience of SA-CQDs. Upon exposure to increasing temperatures from 25 °C to 100 °C, fluorescence intensity decreased only slightly (F/F_0 remained >0.9), and no significant deterioration was observed in the absorbance signal, indicating strong thermal resistance (Figure S5(c)). This stability is attributed to the robust carbon core and the presence of thermally stable functional groups on the CQD

surface [55]. Under continuous UV light irradiation for up to 60 minutes (365 nm), the SA-CQDs retained over 90% of their fluorescence, and the absorbance remained unchanged (Figure S5(d)). This outstanding photostability reflects the durability of the emissive centers and surface states, ensuring that the CQDs can function effectively in long-term or repeated-use sensing scenarios [56].

3.5 *Selective detection of Ag^+*

The selective detection capability of SA-CQDs toward Ag^+ ions was evaluated by monitoring their UV–Vis absorbance response in the presence of various potentially interfering metal ions, each introduced at a concentration of 500 µM. The metal ions tested included Ni^{2+}, Cu^{2+}, Fe^{2+}, Co^{2+}, Bi^{3+}, Pb^{2+}, Hg^{2+}, Cd^{2+}, Cr^{3+}, Sn^{2+}, Zn^{2+}, and Fe^{3+}. As shown in the absorbance spectra, only Ag^+ induced a substantial enhancement in absorption centered at 431 nm, while the other metal ions resulted in negligible or no spectral change (Figure 5(a)). The corresponding visual observation confirmed the unique color development—Ag^+ produced a prominent brownish hue, unlike the colorless or pale appearance of the other samples [17]. Quantitatively, the absorbance intensity ratio (A/A_0) at 431 nm for Ag^+ reached a value significantly higher than that for other ions, with more than a 15-fold increase compared to the baseline, demonstrating excellent optical selectivity (Figure 5(b)).

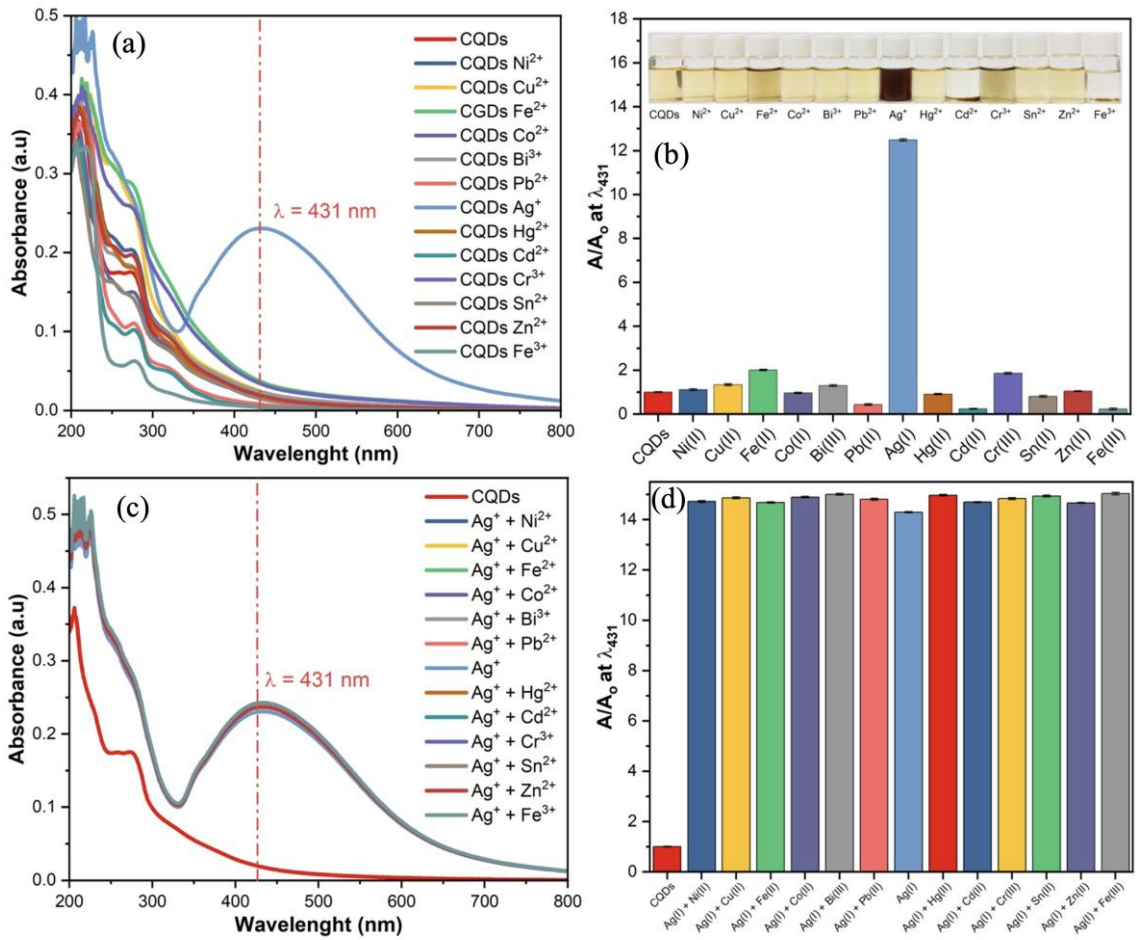

Figure 5: (a) UV–Vis absorbance spectra and (b) A/A_0 intensity ratio of SA-CQDs after treatment with various metal ions (500 µM). (c) Selective absorbance response and (d) corresponding A/A_0 values of SA-CQDs in the presence of Ag^+ and competing metal ions, demonstrating high selectivity.

This behavior is likely attributed to the strong binding affinity between Ag^+ ions and surface functional groups present on the SA-CQDs, including hydroxyl, carboxyl, and amine moieties [18], [57]. These interactions may induce localized aggregation or surface complexation that contributes to new absorbance features. The absence of similar spectral shifts with other cations suggests that the mechanism is highly specific to Ag^+, possibly due to its unique electronic structure and coordination preferences [58]. This selectivity makes SA-CQDs highly promising for use in colorimetric Ag^+ detection in real-world environmental monitoring, where accurate ion discrimination is critical.

To examine the anti-interference capability of SA-CQDs in complex ionic environments, binary mixtures of Ag^+ with other common metal ions were evaluated. Each test solution contained Ag^+ (500 μM) combined with an equimolar amount of a potentially interfering ion, including Ni^{2+}, Cu^{2+}, Fe^{2+}, Co^{2+}, Bi^{3+}, Pb^{2+}, Hg^{2+}, Cd^{2+}, Cr^{3+}, Sn^{2+}, Zn^{2+}, or Fe^{3+}. The absorbance spectra of these mixtures demonstrated that the distinctive peak at 431 nm—induced by the presence of Ag^+—remained largely unchanged despite the coexistence of other ions (Figure 5(c)). Furthermore, the corresponding A/A_0 ratios at 431 nm in all combinations were consistently high and nearly identical to the signal from Ag^+ alone (Figure 5(d)). This indicates that none of the tested ions interfered significantly with the detection response of Ag^+, either by competing for binding sites or inducing similar optical transitions [17], [18], [57]. The robustness of this response suggests a highly selective interaction mechanism between Ag^+ and the surface functionalities of SA-CQDs, likely governed by favorable coordination chemistry and reduction potential differences [58], [59]. It is also possible that the colloidal stability imparted by the SA-CQDs' surface charge (as supported by zeta potential data) prevents nonspecific aggregation in the presence of other cations [19], [20]. These findings confirm the reliability of SA-CQDs in multi-ion systems, a necessary feature for practical deployment in environmental and industrial water monitoring, where metal ion mixtures are common. The combination of high selectivity and strong anti-interference characteristics positions SA-CQDs as a powerful platform for colorimetric Ag^+ sensing applications.

3.6 *Possible mechanism of colorimetric response*

The observed colorimetric response of SA-CQDs upon the addition of Ag^+ ions is believed to originate from a strong interaction between the CQD surface and Ag^+, leading to changes in both the electronic environment and aggregation behavior of the carbon dots. As shown in the fluorescence spectra, the pristine SA-CQDs exhibit intense blue emission with a peak centered at 440 nm under 350 nm excitation. However, upon the introduction of Ag^+ ions, a dramatic quenching of fluorescence is observed, indicating a highly efficient non-radiative decay pathway likely facilitated by surface complexation or charge transfer interactions (Figure 6(a)) [17], [19]. The visual change from a pale yellow to a dark brown solution further supports the occurrence of significant electronic interactions or aggregation phenomena, which alter the light absorption and scattering properties of the system [22], [60]. Time-resolved photoluminescence (TRPL) measurements further confirm the quenching mechanism [20], [60]. The average fluorescence lifetime (τ_{avg}) of SA-CQDs decreased from 3.86 ns to 2.90 ns after the addition of Ag^+ (Figure 6(b) and (c)). This notable reduction suggests that dynamic quenching is involved, potentially through electron transfer from the excited CQDs to Ag^+ ions or via enhanced non-radiative recombination at Ag^+-induced trap states [57]. The presence of Ag^+ may also facilitate the formation of Ag^0 nanoparticles or Ag–CQD hybrid structures, as indicated by the increased absorbance in the 400–500 nm region [21], [61].

To further elucidate the mechanism underlying the colorimetric response of SA-CQDs toward Ag^+ ions, band gap energy and FTIR analyses were conducted. The Tauc plot revealed a significant narrowing of the optical band gap from 4.64 eV in pristine SA-CQDs to 3.81 eV after Ag^+ addition (Figure 6(d) and (e)). This reduction indicates an alteration in the electronic structure, likely due to the introduction of new energy states or enhanced π–π* conjugation as a result of surface coordination or partial reduction of Ag^+ to Ag^0 on the CQDs' surface [21], [23], [61]. Such modifications can facilitate charge transfer interactions and enhance non-radiative decay pathways, contributing to both fluorescence quenching and optical absorbance changes. Complementary FTIR spectra supported this interpretation. The SA-CQDs exhibited characteristic absorption bands corresponding to O–H/N–H

stretching (~3285 cm^{-1}), C=O (~1663 cm^{-1}), aromatic C=C (~1565 cm^{-1}), and C–O (~1108 cm^{-1}) (Figure 6(f)). Upon addition of Ag^+, the intensities of these peaks decreased markedly, particularly in the carbonyl and hydroxyl regions, suggesting direct involvement of these groups in Ag^+ binding [22]. These interactions may cause local structural rearrangement or aggregation, which perturbs the electronic environment of the CQDs and leads to the observed optical responses [20], [60].

Taken together, the sensing mechanism of SA-CQDs toward Ag^+ involves a combination of surface complexation, electron (or charge) transfer, and aggregation-induced quenching, supported by fluorescence lifetime shortening, FTIR peak shifts, and band gap narrowing. While the inner filter effect is less likely due to the absence of overlapping absorption at the excitation/emission range, the formation of Ag^0 or Ag–CQD hybrids may also contribute to the observed optical changes. Therefore, the detection process is primarily governed by dynamic quenching mechanisms involving electron transfer and coordination binding, rather than static absorption-based interference.

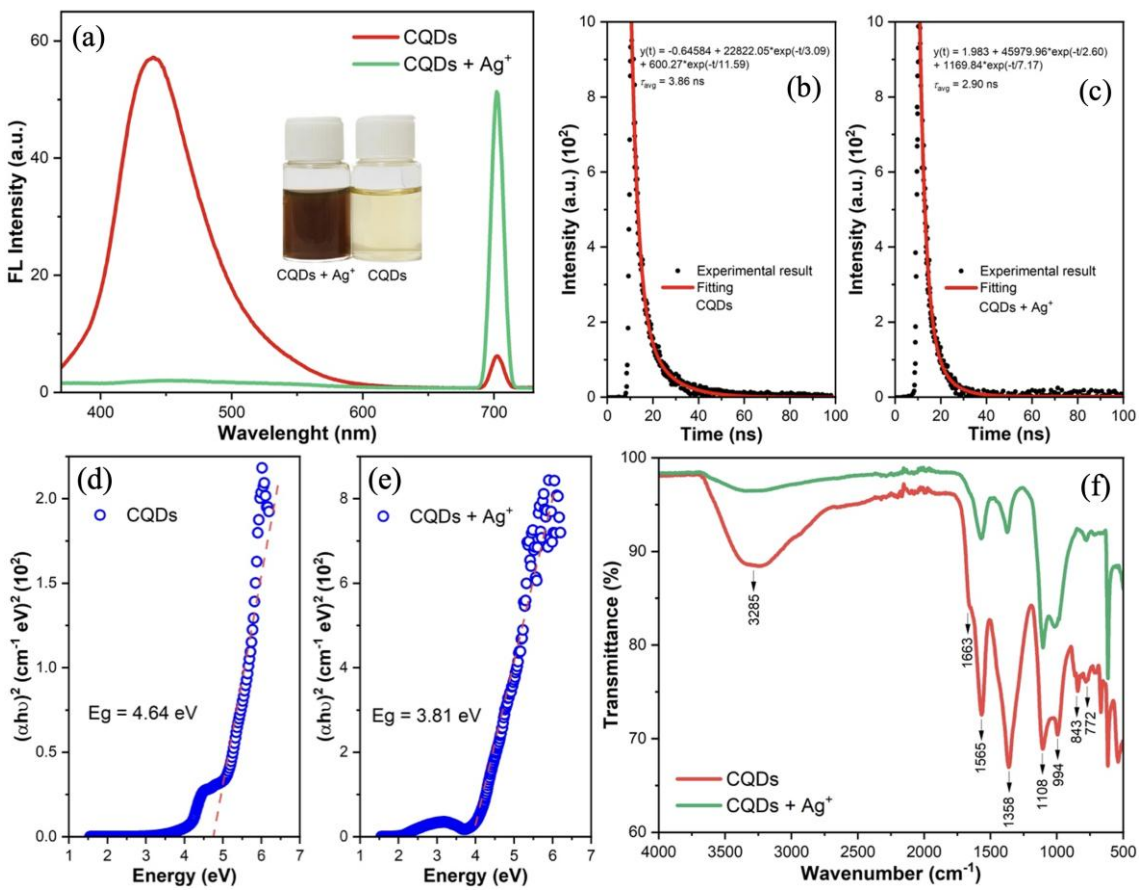

Figure 6: Comparison of optical and chemical properties of SA-CQDs before and after Ag^+ interaction: (a) fluorescence quenching effect, (b–c) fluorescence lifetime decay, (d–e) Tauc plot showing band gap narrowing due to Ag^+ complexation, and (f) FTIR spectra highlighting changes in functional groups post-interaction.

3.7 *Sensitivity of SA-CQDs toward Ag^+ ions*

The sensitivity of SA-CQDs as a colorimetric probe for Ag^+ ions was evaluated by monitoring the absorbance response at 431 nm across a range of Ag^+ concentrations (10–500 µM). As shown in the UV–Vis spectra, the absorbance intensity at λ = 431 nm increased progressively with increasing Ag^+ concentration, accompanied by a distinct color transition from pale yellow to dark brown (Fig. 7a). This visually observable gradient corresponds well with the quantitative response, where the absorbance

intensity ratio (A/A_0) demonstrated a strong linear correlation with Ag^+ concentration, yielding a coefficient of determination (R^2) of 0.95579 (Figure 7(b)). The resulting LOD was found to be 0.103 µM, which corresponds to approximately 0.0111 mg/L (Table 1). This value is well below the maximum permissible silver concentration in drinking water established by the World Health Organization (WHO) at 0.1 mg/L, and also lower than the Canadian Drinking Water Quality guideline of 0.050 mg/L. These results confirm that the SA-CQDs are highly sensitive and suitable for detecting Ag^+ at environmentally and biologically relevant levels [62], [63].

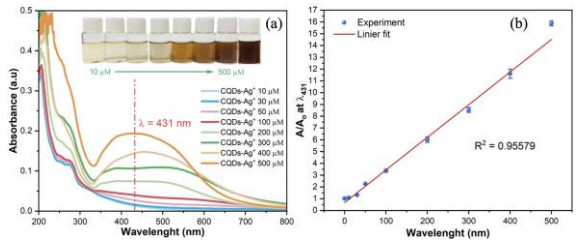

Figure 7: (a) Colorimetric response and (b) linear calibration curve of SA-CQDs for Ag^+ detection at 431 nm.

Table 1: Summary of CQDs synthesized from different carbon precursors for Ag^+ sensing.

No.	Carbon Source	Synthesis Method	Quantum Yield (%)	LOD Values	Ref.
1	Broccoli	Hydrothermal	NA	0.5 µM	[19]
2	Pomegranate juice	Hydrothermal	NA	38×10^{-3} µM	[20]
3	Neem leaves	Pyrolysis and hydrothermal	54	$0.2–0.6 \times 10^3$ µM	[21]
4	*Lycium ruthenicum*	Hydrothermal	21.8	59 nM	[23]
5	Citric and folic acid	Hydrothermal	NA	NA	[60]
6	Sucrose and oleic acid	Hydrothermal	NA	26 nM	[57]
7	Polyurethane	Pyrolysis	33	2.8 µM	[18]
8	Glycine and 2,4-diflouor benzoylacetonitrile	Hydrothermal	20.5 and 42.7	15 nM	[59]
9	*Neera*	Hydrothermal	NA	0.26 mM	[58]
10	Ethyl glycol	Heat treatment	3.02	320 nM	[61]
11	*Syzygium aromaticum*	Carbonization-assisted ultrasonication	12.61	0.103 µM	This work

Table 2: Detection Performance of Ag^+ Ions in Tap and Groundwater Samples (n = 4).

Water Samples	Added (µM)	Measured (µM)	Recovery (%)	RSD (%)
Tap water	10	10.005 ± 0.022	100.05	0.22
	30	29.975 ± 0.091	99.92	0.30
	50	49.965 ± 0.036	99.93	0.07
	100	99.88 ± 0.213	99.88	0.21
	200	199.44 ± 0.442	99.72	0.22
	300	292.43 ± 1.992	97.48	0.68
Underground water	10	9.9875 ± 0.043	99.88	0.43
	30	29.9525 ± 0.047	99.84	0.16
	50	50.04 ± 0.071	100.08	0.14
	100	99.3325 ± 0.431	99.33	0.43
	200	198.055 ± 1.264	99.03	0.64
	300	290.8075 ± 1.877	96.94	0.65

3.8 *Analysis of Ag^+ ions in real water samples*

To assess the practical applicability of the SA-CQDs-based colorimetric sensor for Ag^+ detection, recovery tests were conducted using real water matrices, namely tap water and underground water, with spiked Ag^+ concentrations ranging from 10 to 300 µM (Table 2). As shown in Table 1, the measured concentrations were in excellent agreement with the spiked values, with recoveries ranging from 97.48% to 100.08% for tap water and 96.94% to 100.08% for underground water. At low concentrations (10–100 µM), the recovery rates remained consistently close to 100%, indicating that the sensing system exhibits high sensitivity and precision even at environmentally relevant levels [64]. Only a slight decline in recovery was observed at higher concentrations (300 µM), potentially due to saturation effects or minor matrix interference; however, the performance remained within acceptable analytical error margins [15].

The relative standard deviation (RSD) values for all measurements were below 1%, highlighting the excellent repeatability and precision of the method. The lowest RSD was recorded at 0.07% (50 µM, tap water), while the highest was only 0.68% (300 µM, tap water). These results suggest that SA-CQDs maintain stable and accurate performance in complex aqueous environments without requiring extensive pre-treatment or filtration, underscoring the robustness of the system [65]. Overall, the SA-CQDs sensor demonstrates not only high selectivity and sensitivity under controlled conditions but also excellent

accuracy and reproducibility in real-world samples [66]. This makes the platform highly promising for routine monitoring of silver contamination in drinking water supplies, especially in areas susceptible to heavy metal pollution from industrial or mining activities [67].

4 Conclusions

In this work, a green and efficient approach was employed to synthesize carbon quantum dots (CQDs) using *Syzygium aromaticum* through a carbonization-assisted ultrasonication process. The synthesized SA-CQDs demonstrated strong fluorescent characteristics with a quantum yield of 12.61% and exhibited high specificity in detecting Ag^+ ions, achieving a low detection limit of 0.103 µM. The sensor also displayed excellent environmental stability and reliable performance when applied to real water samples, with recovery rates reaching 100.08% and relative standard deviations (RSDs) of less than 1%. These findings highlight the potential of SA-CQDs as reliable and eco-friendly sensors for monitoring silver contamination in aquatic environments. Future research could explore their adaptation for detecting other toxic metals or biomolecules, surface functionalization for targeted sensing, or integration into portable and paper-based sensing platforms. Moreover, the approach offers promise for scalable green nanomaterial production in fields such as environmental monitoring, food safety, and wastewater treatment.

Acknowledgments

The authors would like to express their gratitude to the Institute for Research and Community Service (LPPM) of Universitas Syiah Kuala for providing financial support for this research.

Author Contributions

S.A.A.: conceptualization and editing; I.Z.: investigation, methodology, writing an original draft; I.S.: research design; Z.J.: conceptualization, data curation, writing—reviewing and editing, funding acquisition, project administration. M.M.R.: data analysis; A.H.L.: investigation, reviewing. All authors have read and agreed to the published version of the manuscript.

Conflicts of Interest

The authors declare no conflict of interest.

References

[1] F. Allambergenova, Z. Smanova, N. Qutlimurotova, A. Abdreymov, F. Sobirova, R. Qutlimurotova, and K. Yakhshinorov, "Synthesis of carbon dots based on chitosan and melamine and their application in detecting vanadate (V) anions," *Chinese Journal of Analytical Chemistry*, vol. 53, no. 7, 2025, Art. no. 100538, doi: 10.1016/j.cjac.2025.100538.

[2] Y. Zhou, W. Zhang, and R. M. Leblanc, "Structure–property–activity relationships in carbon dots," *Journal of Physical Chemistry B*, vol. 126, pp. 10777–10796, 2022, doi: 10.1021/acs.jpcb.2c06856.

[3] H. Wang, Y. Li, Q. Che, X. Liu, S. Zhang, H. Yang, and L. Hu, "Liquid-like carbon dots as lubricating grease additives," *ACS Applied Nano Materials*, vol. 8, pp. 2554–2562, 2025, doi: 10.1021/acsanm.4c06881.

[4] E. G. Amrutha and S. Manivannan, "Carbon dots–based ratiometric fluorescence sensor for hippuric acid," *Physica Status Solidi (A)*, vol. 219, 2022, Art. no. 2200076, doi: 10.1002/pssa.202200076.

[5] P. Venugopalan, N. Vidya, and C. Maya, "Cassia fistula flower extract derived carbon dots for photocatalytic degradation of methylene blue," *International Journal of Environmental Analytical Chemistry*, vol. 104, pp. 7743–7753, 2024, doi: 10.1080/03067319.2023.2182208.

[6] A. Tiron-Stathopoulos and K. Dimos, "Carbon dots' unusual optoelectronic properties in silica aerogels," *Journal of Sol-Gel Science and Technology*, vol. 112, pp. 456–467, 2024, doi: 10.1007/s10971-024-06538-y.

[7] T. Riaz et al., K. M. Alotaibi, and M. Alshalwi, "Carbon dots and nitrogen-doped carbon dots–metal oxide nanocomposites: robust agents for effective sensing of ions," *Journal of Materials Science: Materials in Electronics*, vol. 35, 2024, Art. no. 940, doi: 10.1007/s10854-024-12692-4.

[8] P. Li et al., "Recent advances of carbon dots as new antimicrobial agents," *SmartMat*, vol. 3, pp. 226–248, 2022, doi: 10.1002/smm2.1131.

[9] A. Ferrer-Ruiz, L. Rodríguez-Pérez, N. Martín, and M. Á. Herranz, "Post-synthetic graphitization and photoluminescence tuning of carbon dots

from L-glutamic acid," *Small Structures*, vol. 6, 2025, Art. no. 2400532, doi: 10.1002/sstr.202400532.

[10] W. Xie et al., "Sterically chained amino acid-rich water-soluble carbon quantum dots as a robust tumor-targeted drug delivery platform," *Nature Communications*, vol. 16, 2025, Art. no. 2716, doi: 10.1038/s41467-025-57531-0.

[11] N. Sharma, A. Sharma, and H.-J. Lee, "The antioxidant properties of green carbon dots: a review," *Environmental Chemistry Letters*, 2025, doi: 10.1007/s10311-025-01831-w.

[12] S. A. Akbar, L. Mauliza, and R. R. Fazli, "Recent advances in carbon-based adsorbent materials for ammonium removal from water," *BIO Web of Conferences*, vol. 156, 2025, Art. no. 02014, doi: 10.1051/bioconf/202515602014.

[13] S. A. Akbar and K. Khairunnisa, "Seaweed-based biosorbent for the removal of organic and inorganic contaminants from water: A systematic review," *BIO Web of Conferences*, vol. 87, 2024, Art. no. 02011, doi: 10.1051/bioconf/20248702011.

[14] Gunture and T. Y. Lee, "Biomass-derived multiatom-doped carbon dots for the photocatalytic reduction of Cr(VI) and precipitation of Cr(III)," *NPJ Clean Water*, vol. 7, 2024, Art. no. 132, doi: 10.1038/s41545-024-00426-2.

[15] R. Yadav, V. Lahariya, Vikas, A. K. Singh, A. Das, and A. Yadav, "Fluorometric sensing and nanomolar level detection of heavy metal ions using nitrogen doped carbon dots," *Emergent Materials*, vol. 8, pp. 363–377, 2025, doi: 10.1007/s42247-024-00825-8.

[16] S. A. Akbar, M. Hasan, M. Nazar, I. Zulfahmi, E. Miswar, M. Iqhrammullah, and Z. Jalil, "Fluorescent carbon quantum dots from *Syzygium aromaticum* as a selective sensor for Fe^{3+} and Cd^{2+} detection in aqueous solution," *Case Studies in Chemical and Environmental Engineering*, vol. 11, 2025, Art. no. 101166, doi: 10.1016/j.cscee.2025.101166.

[17] G. R. Tortella, O. Rubilar, N. Durán, M. C. Diez, M. Martínez, J. Parada, and A. B. Seabra, "Silver nanoparticles: Toxicity in model organisms as an overview of its hazard for human health and the environment," *Journal of Hazardous Materials*, vol. 390, 2020, Art. no. 121974, doi: 10.1016/j.jhazmat.2019.121974.

[18] M. I. S. D. Cruz, N. Thongsai, M. D. G. de Luna, I. In, and P. Paoprasert, "Preparation of highly photoluminescent carbon dots from polyurethane: Optimization using response surface methodology and selective detection of silver (I) ion," *Colloids and Surfaces A: Physicochemical and Engineering Aspects*, vol. 568, pp. 184–194, 2019, doi: 10.1016/j.colsurfa.2019.02.022.

[19] N. Arumugam and J. Kim, "Synthesis of carbon quantum dots from broccoli and their ability to detect silver ions," *Materials Letters*, vol. 219, pp. 37–40, 2018, doi: 10.1016/j.matlet.2018.02.043.

[20] S. A. Akbar, M. Hasan, Z. Jalil, I. Zulfahmi, M. Iqhrammullah, and N. Safina, "Enhanced ammonia nitrogen filtration using NaOH-activated *Manihot utilissima* peel carbon: Application in recirculating aquaculture systems for Nile tilapia," *Chemosphere*, vol. 385, 2025, Art. no. 144537, doi: 10.1016/j.chemosphere.2025.144537.

[21] A. Suryawanshi et al., "Large scale synthesis of graphene quantum dots (GQDs) from waste biomass and their use as an efficient and selective photoluminescence on–off–on probe for Ag^+ ions," *Nanoscale*, vol. 6, pp. 11664–11670, 2014, doi: 10.1039/C4NR02494J.

[22] P. Murugesan, N. Libiya, J. A. Moses, and C. Anandharamakrishnan, "Fluorescence resonance energy transfer-based sensor with silver-conjugated orange peel waste-derived carbon dots for melamine detection," *Carbon Letters*, vol. 33, pp. 2335–2348, 2023, doi: 10.1007/s42823-023-00563-7.

[23] S. Tang et al., "A smartphone-integrated optical sensing platform based on *Lycium ruthenicum* derived carbon dots for real-time detection of Ag^+," *Science of The Total Environment*, vol. 825, 2022, Art. no. 153913, doi: 10.1016/j.scitotenv.2022.153913.

[24] F. El-akhal et al., "Phytochemical screening, chemical composition and larvicidal efficacy of *Syzygium aromaticum* extracts and essential oil against *Culex pipiens*," *Tropical Journal of Natural Product Research*, vol. 8, pp. 5962–5967, 2024, doi: 10.26538/tjnpr/v8i1.35.

[25] R. Kumar, V. B. Kumar, and A. Gedanken, "Sonochemical synthesis of carbon dots, mechanism, effect of parameters, and catalytic, energy, biomedical and tissue engineering applications," *Ultrasonics Sonochemistry*, vol. 64, 2020, Art. no. 105009, doi: 10.1016/j.ultsonch.2020.105009.

[26] I. Diwan and G. K. Tripathi, and P. S. Khare, "Synthesis of green fluorescent, energy efficient nitrogen doped carbon quantum dots," *Optik*, vol. 303, 2024, Art. no. 171725, doi: 10.1016/j.ijleo.2024.171725.

[27] S. K. Saraswat et al., "Carbon quantum dots: A comprehensive review of green synthesis, characterization and investigation their applications in bioimaging," *Inorganic Chemistry Communications*, vol. 162, 2024, Art. no. 112279, doi: 10.1016/j.inoche.2024.112279.

[28] V. A. Sadhu, T. J. Park, and S. K. Kailasa, "Synthesis of green fluorescent carbon dots using cysteine and maltose as ecofriendly ligands for the detection of venlafaxine anti-depression drug in pharmaceutical and plasma samples," *Inorganic Chemistry Communications*, vol. 168, 2024, Art. no. 112980, doi: 10.1016/j.inoche.2024.112980.

[29] X. Long, H. Liu, J. Hu, and S. Wu, "Green synthesis of N,S dual heteroatom-doped fluorescent carbon dots (N,S-CDs) and their applications in gentamicin sensing and dual-switch anti-counterfeiting encryption," *Dyes and Pigments*, vol. 231, 2024, Art. no. 112413, doi: 10.1016/j.dyepig.2024.112413.

[30] J.-H. Mou et al., "Green synthesis of lactic acid and carbon dots using food waste and seashell waste," *Green Chemistry*, vol. 26, pp. 8282–8297, 2024, doi: 10.1039/d4gc01890g.

[31] N. Sharma et al., "Green hydrothermal approach for the synthesis of carbon quantum dots from waste tea bags for acrylamide detection in drinking water: A fluorescence assay validated by HPLC-PDA analysis," *Food Chemistry: X*, vol. 25, 2025, Art. no. 102043, doi: 10.1016/j.fochx.2024.102043.

[32] M. Gagana et al., "Green synthesis of carbon dots encapsulated MoO_3:La^{3+} for enhanced photocatalytic degradation, dactyloscopy and real-time FP detection using YOLOv8x," *Journal of the Taiwan Institute of Chemical Engineers*, vol. 170, 2025, Art. no. 106032, doi: 10.1016/j.jtice.2025.106032.

[33] A. Daulay et al., "Green sources for carbon dots synthesis in sensing for food application – A review," *Biosensors and Bioelectronics: X*, vol. 17, 2024, Art. no. 100460, doi: 10.1016/j.biosx.2024.100460.

[34] S. Patra, A. K. Golder, and R. V. S. Uppaluri, "Green synthesis of carbon dots from mature green tea leaves for label-free fluorescence sensing of chromium(VI)," *Optical Materials*, vol. 154, 2024, Art. no. 115767, doi: 10.1016/j.optmat.2024.115767.

[35] C. W. Backes, F. B. Reis, G. B. Strapasson, M. Assis, E. Longo, and D. E. Weibel, "Green synthesis of carbon quantum dots for enhancing photocatalytic activity: Hydrogen/oxygen evolution and dye photodegradation," *Catalysis Today*, vol. 443, 2025, Art. no. 114996, doi: 10.1016/j.cattod.2024.114996.

[36] H. Chen, G. Huang, Y. Li, and Y. Huang, "In situ green synthesis of *Rosa sterilis*-based carbon dots for Fe^{3+} fluorescent sensing in baijiu," *Food Bioscience*, vol. 62, 2024, Art. no. 105403, doi: 10.1016/j.fbio.2024.105403.

[37] I. B. Raval, V. N. Mehta, S. Jha, T. J. Park, and S. K. Kailasa, "Synthesis of green emissive *Plectranthus scutellarioides* carbon dots for sustainable and label-free detection of phytohormone indole-3-acetic acid," *Inorganic Chemistry Communications*, vol. 171, 2025, Art. no. 113660, doi: 10.1016/j.inoche.2024.113660.

[38] M. Idrees, N. Saqib, and G. Zaman, "Green synthesis of carbon dots (CDs) and their use for selective determination of Pb^{2+}," *Spectrochimica Acta Part A: Molecular and Biomolecular Spectroscopy*, vol. 326, 2025, Art. no. 125303, doi: 10.1016/j.saa.2024.125303.

[39] Y. Yu et al., "Green synthesis of carbon quantum dots from nutshells for enhanced performance in dye-sensitized solar cells," *RSC Advances*, vol. 15, pp. 7938–7947, 2025, doi: 10.1039/d4ra08649j.

[40] C. O. Ugwuoke, M. Ghali, and A. A. El-Moneim, "Green synthesis of carbon dots from *Nigella sativa* seeds for supercapacitor application," *Journal of Energy Storage*, vol. 95, 2024, Art. no. 112634, doi: 10.1016/j.est.2024.112634.

[41] Z. Li, Z. Miao, J. Shen, J. Wang, and L. Lin, "Green synthesis of carbon dots by microflow method and their application as sunscreen agent," *Chinese Journal of Chemical Engineering*, vol. 77, pp. 135–143, 2025, doi: 10.1016/j.cjche.2024.10.008.

[42] I. Chen, T. Li, C. Lin, Y. Hou, S. Cheng, and B. Gao, "Green synthesis of red-emitting carbon dots for bioimaging, sensing, and antibacterial applications," *Spectrochimica Acta Part A: Molecular and Biomolecular Spectroscopy*, vol. 328, 2025, Art. no. 125458, doi: 10.1016/j.saa.2024.125458.

[43] V. Renuga et al., "Green synthesis of biocompatible fluorescent carbon dots from bitter gourd for

effective metal sensing and biological applications," *Sensing and Bio-Sensing Research*, vol. 47, 2025, Art. no. 100751, doi: 10.1016/j.sbsr.2025.100751.

[44] J. Hu and S. Wu, "Green and sustainable synthesis of fluorescent carbon dots from crown daisy for information encryption application," *Journal of Molecular Structure*, vol. 1324, 2025, Art. no. 140794, doi: 10.1016/j.molstruc.2024.140794.

[45] S. K. Kalifathullah, S. Alaguvel, and D. Sundaramurthy, "Efficient synthesis of green nitrogen-doped carbon dots as a versatile nanoprobe for antibacterial, cytotoxic, in-vitro imaging, and anti-counterfeit applications," *Inorganic Chemistry Communications*, vol. 178, 2025, Art. no. 114473, doi: 10.1016/j.inoche.2025.114473.

[46] H. K. Kohli and D. Parab, "Green synthesis of carbon quantum dots and applications: An insight," *Next Materials*, vol. 8, 2025, Art. no. 100527, doi: 10.1016/j.nxmate.2025.100527.

[47] B. I. Salman, H. A. Batakoushy, R. E. Saraya, A. I. Hassan, A. Al-Harrasi, and A. E. Ibrahim, "Comprehensive investigation of *Prunus armeniaca* for natural green synthesis of carbon quantum dots; Applications as fluorescent nano-probes for ramipril," *Talanta*, vol. 292, 2025, Art. no. 128014, doi: 10.1016/j.talanta.2025.128014.

[48] I. Ramajayam and A. Palaniappan, "Facile and green synthesis of highly fluorescent boron and nitrogen-doped carbon dots (BN-CDs) for the fluorimetric detection of Au^{3+} ions in aqueous media and in in vitro cell imaging," *Colloids and Surfaces A: Physicochemical and Engineering Aspects*, vol. 709, 2025, Art. no. 136062, doi: 10.1016/j.colsurfa.2024.136062.

[49] R. Ali et al., "A novel red emissive glutathione-capped carbon dots embedded within molecularly-imprinted polymers for adsorption and fluorescent sensing of malachite green in food samples," *Microchemical Journal*, vol. 212, 2025, Art. no. 113376, doi: 10.1016/j.microc.2025.113376.

[50] H. Xu, W. Zhan, M. Wan, X. Bao, and L. Tang, "Research on green synthesis and performance analysis of biomass-derived carbon quantum dots," *Industrial Crops and Products*, vol. 227, 2025, Art. no. 120775, doi: 10.1016/j.indcrop.2025.120775.

[51] W. Zhang et al., "A universal sensing platform based on iron and nitrogen co-doped carbon dots for detecting hydrogen peroxide and related metabolites in human fluid by ratiometric fluorometry and colorimetry," *Spectrochimica Acta Part A: Molecular and Biomolecular Spectroscopy*, vol. 272, 2022, Art. no. 121003, doi: 10.1016/j.saa.2022.121003.

[52] D. Yang, T. Shao, L. Zhang, X. Wang, and Q. Yue, "Novel carbon dots from phenylenediamine for simultaneous detection of peroxydisulfate and phosphate with a smartphone by dual-channel of fluorometry and colorimetry," *Food Chemistry*, vol. 472, 2025, Art. no. 142905, doi: 10.1016/j.foodchem.2025.142905.

[53] H. Wang et al., "Gadolinium-doped carbon dots as a ratiometric fluorometry and colorimetry dual-mode nano-sensor based on specific chelation for morin detection," *Sensors and Actuators B: Chemical*, vol. 352, 2022, Art. no. 130991, doi: 10.1016/j.snb.2021.130991.

[54] X.-H. Duan, H.-W. Li, and Y. Wu, "A smart ratiometric fluorescence and colorimetry dual-responsive sensor for morin determination based on the complex between carbon quantum dots and polyethyleneimine," *Analytica Chimica Acta*, vol. 1243, 2023, Art. no. 340814, doi: 10.1016/j.aca.2023.340814.

[55] Y. Kong, T. Lei, Y. He, and G. Song, "Background-free room temperature phosphorescence and digital image colorimetry detection of melamine by carbon nitride quantum dots in cellulose matrix with smartphone-based portable device," *Food Chemistry*, vol. 390, 2022, Art. no. 133135, doi: 10.1016/j.foodchem.2022.133135.

[56] Q. Chen et al., "Ratio fluorescence and smartphone-assisted colorimetry dual-mode detection of creatinine based on F, B, N-doped of red fluorescent carbon dots," *Analytica Chimica Acta*, vol. 1349, 2025, Art. no. 343815, doi: 10.1016/j.aca.2025.343815.

[57] J.-C. Jin et al., "A novel method for the detection of silver ions with carbon dots: Excellent selectivity, fast response, low detection limit and good applicability," *Sensors and Actuators B: Chemical*, vol. 267, pp. 627–635, 2018, doi: 10.1016/j.snb.2018.04.036.

[58] P. Murugesan, J. A. Moses, and C. Anandharamakrishnan, "One step synthesis of fluorescent carbon dots from neera for the detection of silver ions," *Spectroscopy Letters*,

vol. 53, pp. 407–415, 2020, doi: 10.1080/00387010.2020.1764589.

[59] J. Guo, S. Ye, H. Li, J. Song, and J. Qu, "Novel carbon dots with dual excitation for imaging and silver ion detection in living cells," *Dyes and Pigments*, vol. 183, 2020, Art. no. 108723, doi: 10.1016/j.dyepig.2020.108723.

[60] I. Gontrani, E. M. Bauer, A. Nucara, P. Tagliatesta, and M. Carbone, "Highly specific silver ion detection by fluorescent carbon quantum dots," *Chemosensors*, vol. 10, 2022, Art. no. 90362, doi: 10.3390/chemosensors 10090362.

[61] X. Gao et al., "One-pot synthesis of carbon nanodots for fluorescence turn-on detection of Ag^+ based on the Ag^+-induced enhancement of fluorescence," *Journal of Materials Chemistry C*, vol. 3, pp. 2302–2309, 2015, doi: 10.1039/C4TC02582B.

[62] I. Marcus, "Testing above the limit: Drinking water contamination and test scores," *Journal of Public Economics*, vol. 243, 2025, Art. no. 105313, doi: 10.1016/j.jpubeco.2025.105313.

[63] L. Ogisma, F. C. O'Donnell, W. Sawadgo, J. J. Molnar, G. Huluka, and E. Laguerre, "Pricing drinking water testing in northern Haiti: Financial sensitivity to operating costs, user demand, and economic conditions," *Heliyon*, vol. 10, 2024, Art. no. e38063, doi: 10.1016/j.heliyon.2024.e38063.

[64] W. Zhong and J. Yang, "Fluorescent carbon quantum dots for heavy metal sensing," *Science of The Total Environment*, vol. 957, 2024, Art. no. 177473, doi: 10.1016/j.scitotenv.2024.177473.

[65] C. Tian et al., "Machine-learning-enhanced fluorescent nanosensor based on carbon quantum dots for heavy metal detection," *ACS Applied Nano Materials*, vol. 7, 2024, Art. no. 5576–5586, doi: 10.1021/acsanm.4c00359.

[66] V. Chobpattana, T. Sangtawesin, P. Khaopueak, and K. Wechakorn, "Sugar derived-fluorescent carbon quantum dots conjugated glutathione for sensing heavy metal ions and antioxidant activity," *Materials Science and Engineering: B*, vol. 313, 2025, Art. no. 117956, doi: 10.1016/j.mseb.2024.117956.

[67] H. Javeria, M. Q. Abbas, S.-H. Chen, B. E. Keshat, and Z. Du, "Scalability of sulfur-functionalized carbon quantum dots from peanut shells: A sustainable sensor of high colorimetric heavy metal detection," *Journal of Environmental Chemical Engineering*, vol. 13, 2025, Art. no. 115821, doi: 10.1016/j.jece.2025.115821.

Supporting Information

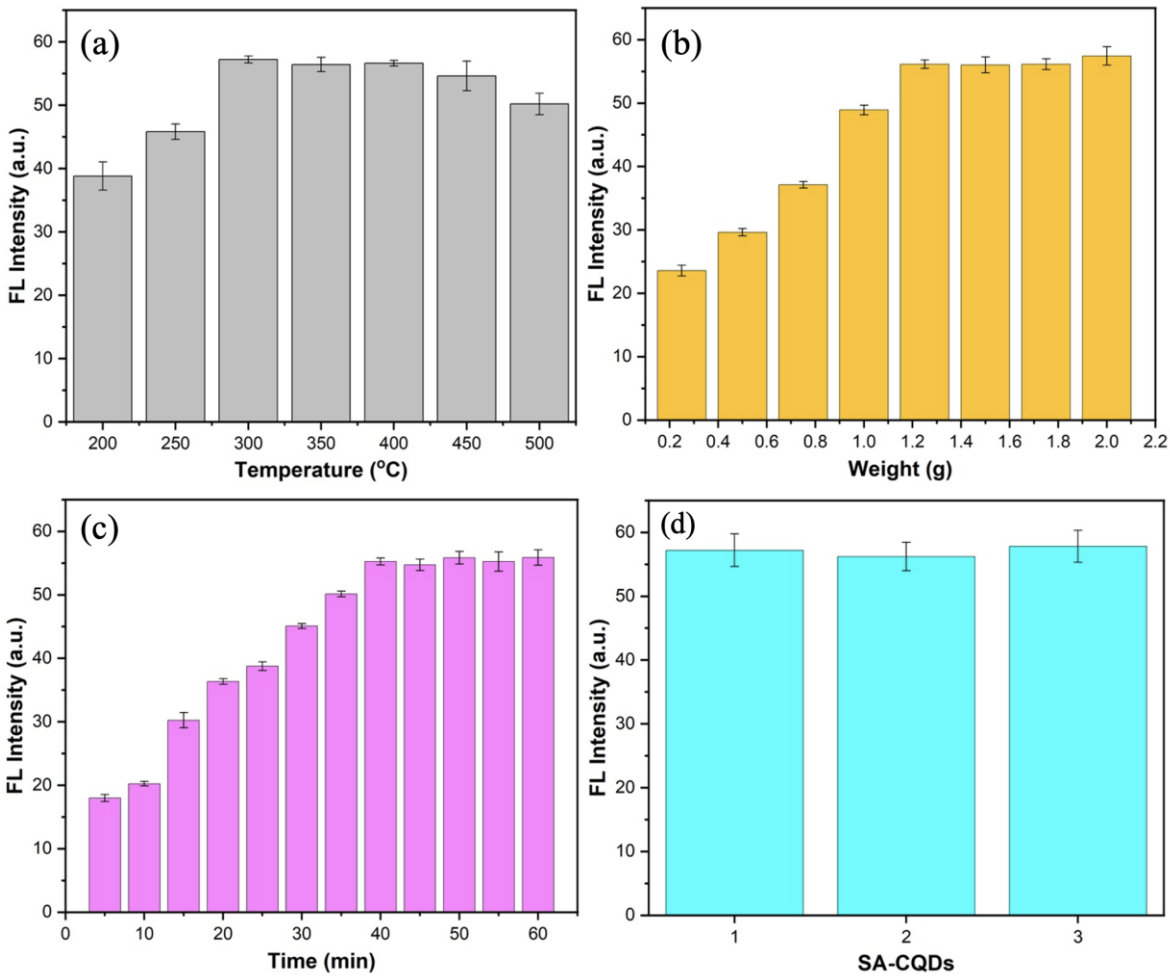

Figure S1: Comparison of SA-CQDs synthesized under varying conditions: (a) carbonization temperatures (200, 250, 300, 350, 400, 450, and 500 °C) for 2 h, (b) mass of *Syzygium aromaticum* (0.25, 0.5, 0.75, 1.0, 1.25, 1.5, 1.75, and 2.0 g) at a carbonization temperature of 300 °C for 2 h, (c) sonication durations (5, 10, 15, 20, 25, 30, 35, 40, 45, 50, 55, and 60 min) at a carbonization temperature of 300 °C for 2 h using 1.25 g of carbonized SA powder, and (d) FL intensity under the optimized synthesis conditions (carbonization temperature of 300 °C for 2 h, 1.25 g of SA powder, 30-min sonication) with an excitation wavelength of 350 nm and emission wavelength of 440 nm.

Table S1: Lattice spacing and crystallographic planes of SA-CQDs from SAED analysis.

No.	Label	1/2r (nm^{-1})	1/r (nm^{-1})	r (nm)	d-spacing (Å)	(hkl)
1	Acquire SAED.tif	6.002	3.001	0.333222	3.332222592	(002)
2	Acquire SAED.tif	8.498	4.249	0.235349	2.35349494	(100)

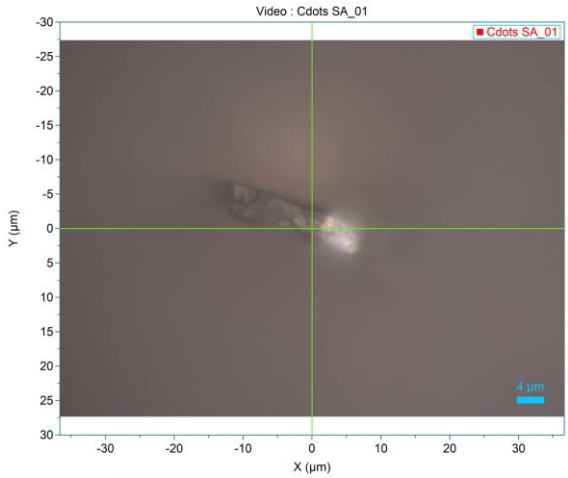

Figure S2: Optical microscopy image of SA-CQDs during raman spectroscopy measurement.

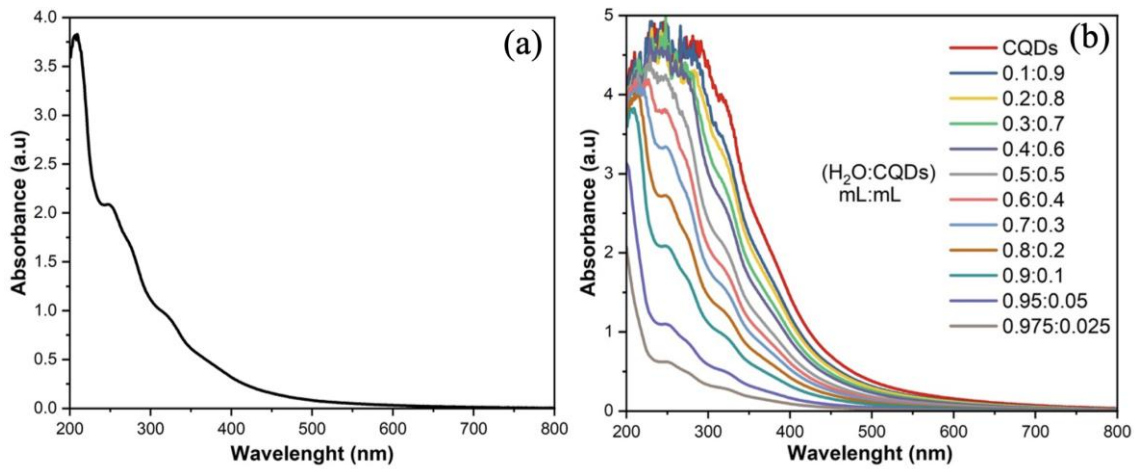

Figure S3: (a) UV–vis spectrum of SA-CQDs and (b) UV–vis spectra of SA-CQDs solutions with different dilution factors.

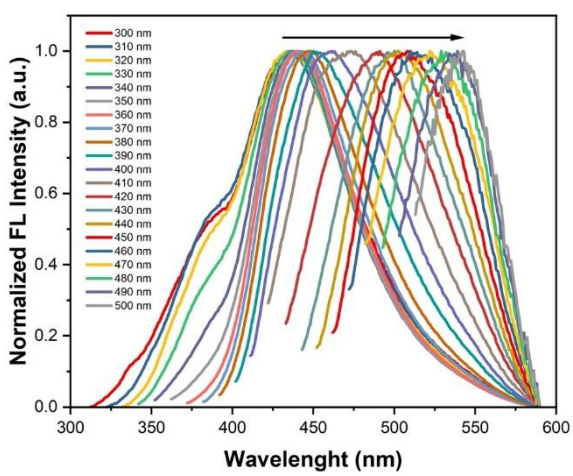

Figure S4: Normalized FL spectra of SA-CQDs at various excitation wavelengths from 300 to 500 nm with a 20 nm increase.

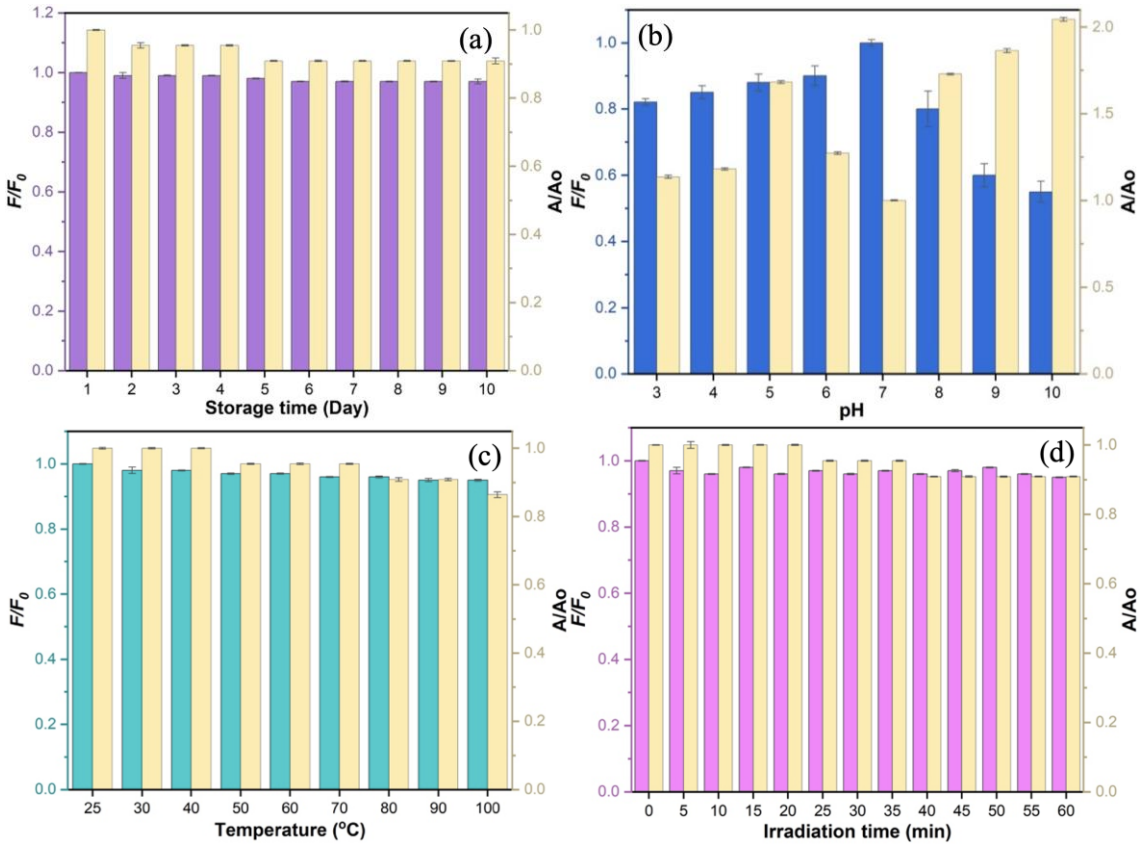

Figure S5: Optical stability of SA-CQDs under various environmental conditions (a) storage time, (b) pH, (c) temperature, and (d) light irradiation.

Quantum Yield Calculation

$$QY_x = QY_y \left(\frac{A_y}{A_x}\right)\left(\frac{I_x}{I_y}\right)\left(\frac{\eta_x^2}{\eta_y^2}\right)$$

Fluorescence and absorbance measurements at 350 nm for *Syzygium aromaticum*

- Refractive index (η) = 1.33
- Absorbance at 350 nm (A) = 0.05
- Fluorescence intensity at 350 nm (I) = 57.234

Fluorescence and absorbance measurements at 350 nm for quinine

- Refractive index (η) = 1.33
- Absorbance at 350 nm (A) = 0.05
- Fluorescence intensity at 350 nm (I) = 245.04
- Quantum Yield (QY) = 54%

$$QY_x = 54\left(\frac{0.05}{0.05}\right)\left(\frac{57.234}{245.04}\right)\left(\frac{1.33^2}{1.33^2}\right)$$

= 12.61%